Electronic Supplementary Material (ESI) for RSC Advances.
This journal is © The Royal Society of Chemistry 2024

Electronic Supplementary Information

for

Efficient photoactivated hydrogen evolution promoted by Cu_xO-gCN-TiO_2-Au (x=1,2) nanoarchitectures

Mattia Benedet,[a,b] Gian Andrea Rizzi,[a,b] Alberto Gasparotto,[a,b] Lunjie Zeng,[c] Gioele Pagot,[d] Eva Olsson,[c] Vito Di Noto,[d] Chiara Maccato,[a,b,*] and Davide Barreca[b]

[a] *Department of Chemical Sciences, Padova University and INSTM, 35131 Padova, Italy*

[b] *CNR-ICMATE and INSTM, Department of Chemical Sciences, Padova University, 35131 Padova, Italy*

[c] *Department of Physics, Chalmers University of Technology, 41296 Gothenburg, Sweden*

[d] *Section of Chemistry for the Technology (ChemTech), Department of Industrial Engineering - Padova University and INSTM, 35131 Padova, Italy*

* Corresponding author. E-mail: chiara.maccato@unipd.it.

Table of Contents

§ S-1. Experimental

§ S-1.1. Chemico-physical characterization

X-ray diffraction (XRD) was performed in glancing incidence mode (θ_i = 1.0°) on a Bruker AXS D8 Advance Plus diffractometer, equipped with a Göbel mirror and a CuKα X-ray source (λ = 1.54051 Å) powered at 40 kV and 40 mA. The analyses were carried out at the PanLab facility (Department of Chemical Sciences, Padova University) founded by the MIUR Dipartimento di Eccellenza grant "NExuS".

Copper Auger parameter was calculated as the sum of Cu $2p_{3/2}$ BE and the Cu *LMM* Auger peak kinetic energy (KE):[1, 2]

$$\alpha = BE(Cu\ 2p_{3/2}) + KE(Cu\ LMM) \quad (S1)$$

Elemental atomic percentage (at.%) values were computed by peak area integration, using sensitivity factors provided by Specs.

Cross-sectional samples for transmission electron microscopy (TEM) analyses were prepared using a FEI Versa3D focus ion beam-scanning electron microscope (FIB-SEM). The final polishing of TEM specimens was performed using a Ga ion beam, under conditions enabling to minimize detrimental material alterations (energy = 2 kV; beam current ≈ 25 pA).

§ S-1.2. Functional tests

Current density values were obtained by dividing the measured currents for the exposed geometric area (≈ 1.20 cm^2). In fact, for materials as the present ones, BET measurements of the real active area and a reliable evaluation of electrochemical active surface area (ECSA) are not possible, as already reported.[3-5]

The potential of the Hg/HgO (MMO) reference electrode was periodically recalibrated after tests and no significant variation with respect to RHE was ever detected, ensuring thus a full reproducibility of the obtained results.

Linear sweep voltammetry (LSV) curves were collected at a scan rate of 5 mV/s. The potential values *vs.* MMO (E_{MMO}) were converted into the corresponding ones on the reversible hydrogen electrode (RHE) scale (E_{RHE}) using the relation:

$$E_{RHE}\,(V) = E_{MMO}\,(V) + 0.0592 \times pH + 0.075 \quad (S2)$$

Applied bias photon-to-current efficiency (ABPE) (%) curves were obtained through the equation:[6]

$$ABPE\ (\%) = (|j \times E|\ /\ P) \times 100 \quad (S3)$$

were j (mA/cm^2) is the photocurrent density at the potential E (V *vs.* RHE), and P is the incident light intensity (100 mW/cm^2). In this work, all the reported j values (including those in Tables S1-S2), apart from the case of Fig. 9 that displays the current densities as such, are calculated as the difference between the values recorded under illumination and in the dark.

For all the performed photoelectrochemical tests, a neutral white LED (220 lm, 700 mA) has been employed (Fig. S1). In a typical experiment, the sample was illuminated from the front side with the maximum light intensity (corresponding to an input current of 700 mA) at a distance of 10 cm from the specimen surface. In order to obtain quantitative results, the light source intensity was periodically re-calibrated prior to measurements.

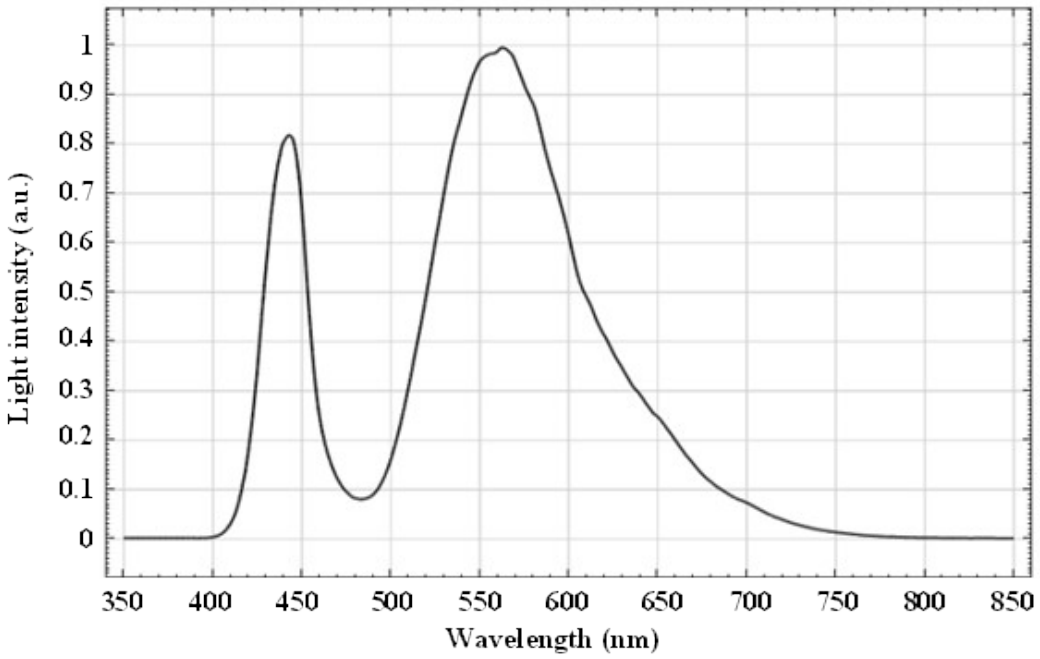

Fig. S1. Spectrum of the light source employed for photoelectrochemical tests. The light intensity in the Y axis is scaled to the maximum at $\lambda \approx 560$ nm.

Electrochemical impedance spectroscopy (EIS) experiments were carried out between 1 and 10^5 Hz with a 10 mV perturbation. Mott-Schottky plots were obtained at 1.0 kHz by recording EIS

spectra between 0.0 and 0.6 V *vs*. RHE, with 0.05 V steps. The flatband potential (V_{FB}) was measured by fitting the linear part of $1/C_{SC}^2$ and finding the intercept with the potential axis, using the equation:[7-10]

$$\frac{1}{C_{sc}^2} = \frac{2}{\varepsilon_0 \varepsilon_r e N_A}\left(V - V_{FB} - \frac{k_B T}{e}\right) \quad \text{(S4)}$$

where C_{SC} is the semiconductor capacitance (the contribution of the double layer capacitance, $1/C_H^2$, is considered negligible), ε_0 and ε_r are the free space permittivity and the material relative permittivity, e is the electron charge (C), N_A is the majority carrier density, V is the applied bias, and k_B is the Boltzmann constant. The capacitance C_{SC} was calculated at 1054 Hz by using the usual formula:

$$Z'' = -\frac{i}{C_{sc} \cdot \omega} \quad \text{(S5)}$$

where Z'' is the complex component of the measured impedance. The Fermi level energy (E_F) was assumed to be coincident with V_{FB}, and was used to construct the diagram reported in Fig. 4e. The E_F value in Fig. 4e corresponds to V_{FB} of sample Cu_xO-gCN-TiO_2-Au (purple line in Fig. 4d and S11).

Chronoamperometry (CA) measurements were performed by recording the photocurrent as a function of time at 0.0 V *vs.* RHE.

Preliminary photoreforming experiments for H_2 generation were performed from 1:1 water-ethanol mixtures, using a previously described reactor[11] stabilized at 25°C and purged for ≈ 30 min with an Ar flow (rate = 15 mL/min) prior to measurements. Irradiation was carried out using a solar simulator (Lot-Oriel) equipped with a 150 W Xe lamp and an atmospheric edge filter. The on-line detection of the evolved hydrogen was carried out using an Agilent 7890A gas chromatographer. A Carboxen 1010 PLOT column (Supelco) connected to a thermal conductivity detector was adopted for H_2 quantification, using Ar as carrier. Based on the sample geometrical area (see above), H_2 production rates were expressed as mmol h^{-1} m^{-2}.[11, 12] Prof. Paolo Fornasiero and Dr. Valentina Gombac (Department of Chemical and Pharmaceutical Sciences, Trieste University and INSTM, Italy) are gratefully acknowledged for such tests.

§ S-2. Additional characterization results

§ S-2.1. Characterization of the obtained systems

FE-SEM and EDXS analyses of sample Cu_xO-gCN (Fig. S2a-b and S3) clearly displayed the formation of a porous gCN overlayer. The presence of Cu_xO nanowires was still evident, despite in an apparently lower concentration in comparison to the pristine Cu_xO (compare Fig. 1b-e in the main paper text). These variations in the system morphology can be ascribed to a partial coverage and embedding of copper oxide nanowires into the deposited gCN matrix, which is maintained even after TiO_2 and Au introduction by RF-Sputtering (see Fig. S2c). The inherent porosity of the starting copper foam and the adopted synthetic strategy, with particular regard to the RF-Sputtering infiltration capability, favor an intimate intermixing of the single system components, beneficially affecting the ultimate functional performances (see the main paper text).

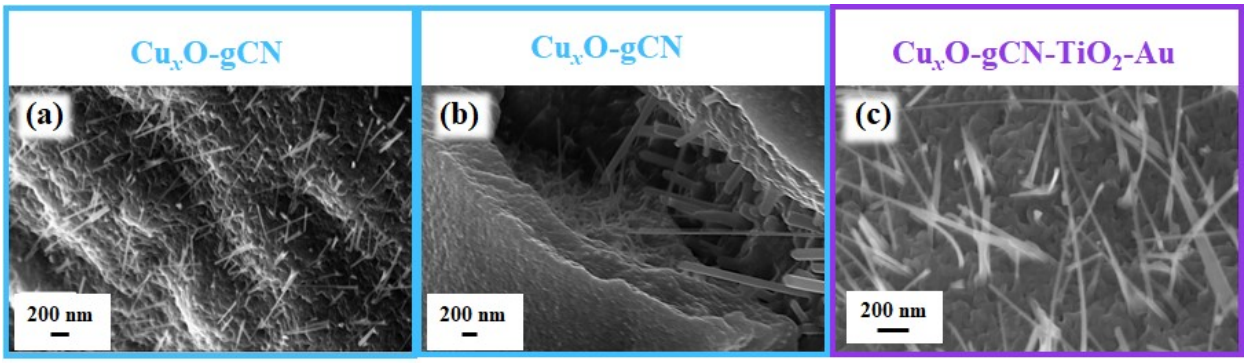

Fig. S2. Representative FE-SEM micrographs for Cu_xO-gCN and Cu_xO-gCN-TiO_2-Au photoelectrocatalysts.

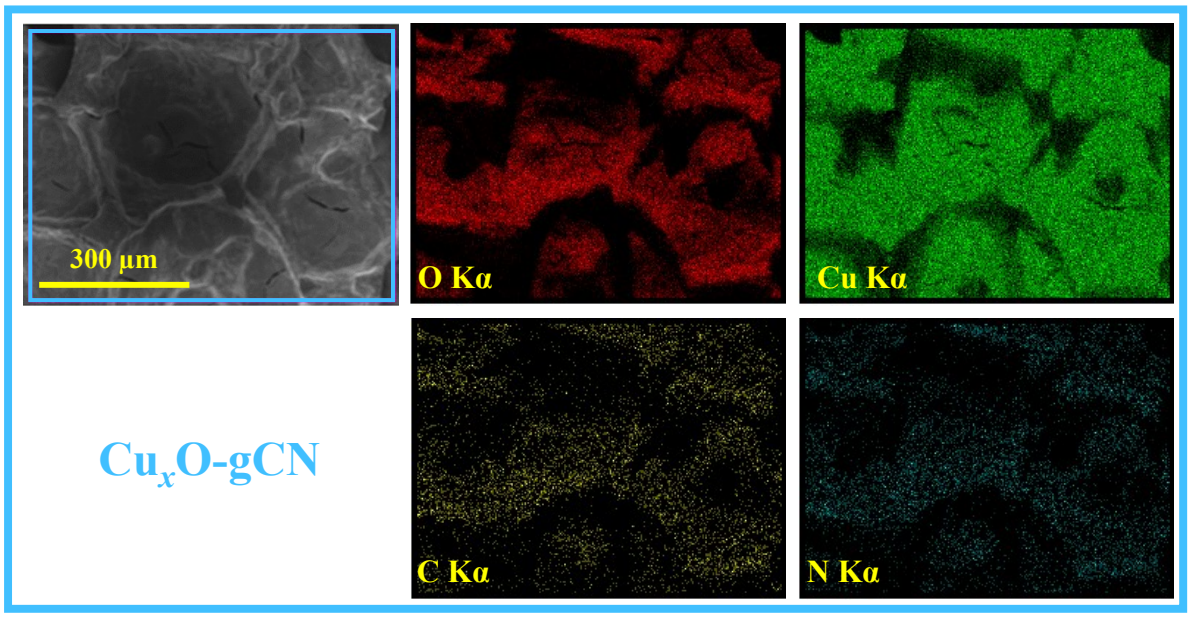

Fig. S3. EDXS O, Cu, C, and N elemental maps for sample Cu_xO-gCN, recorded on the electron image displayed in the top left corner.

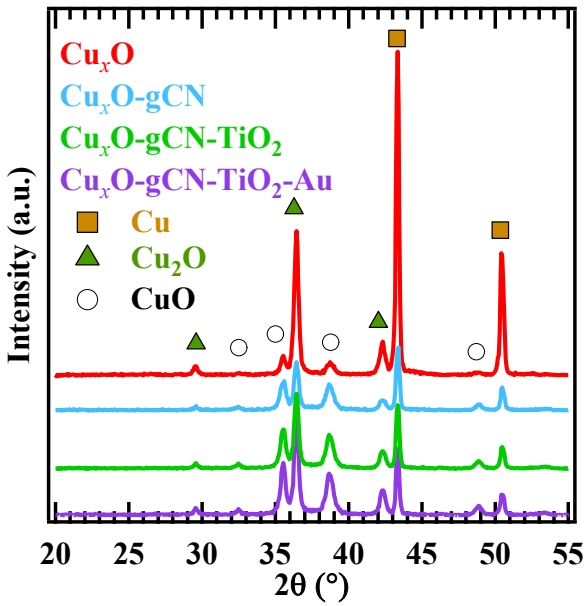

Fig. S4. XRD patterns for the target specimens. The reference peak positions for Cu,[13] Cu_2O,[14] and CuO[15] are marked by squares, triangles, and circles, respectively.

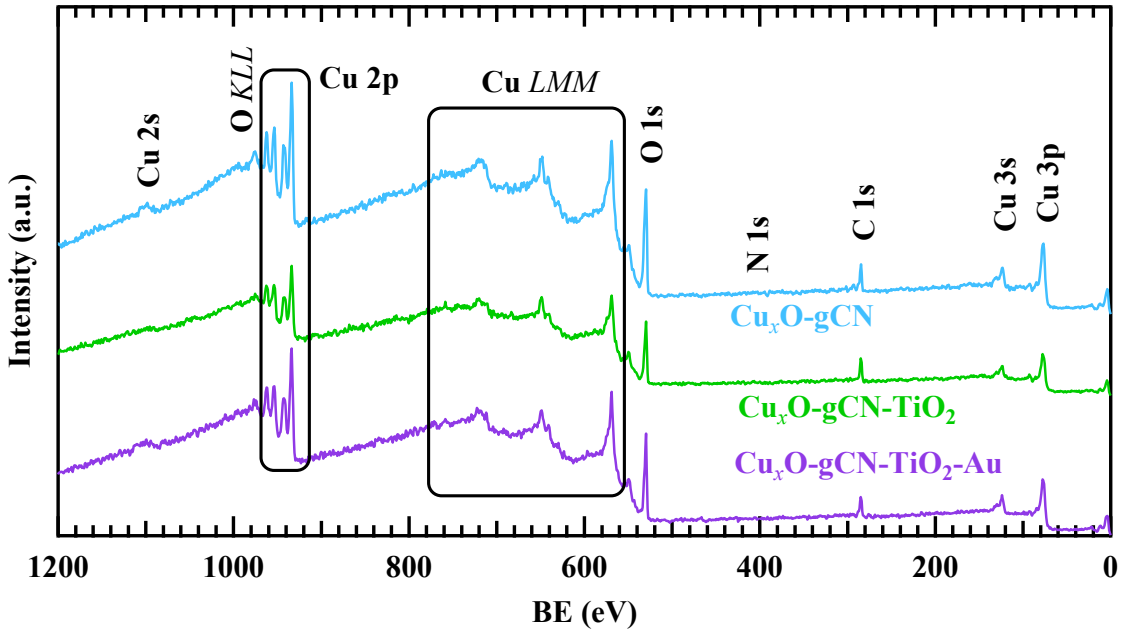

Fig. S5. XPS survey spectra for Cu_xO-gCN, Cu_xO-gCN-TiO_2 and Cu_xO-gCN-TiO_2-Au. For both composite systems, the measured N/Cu atomic percentage ratio corresponds to 0.030.

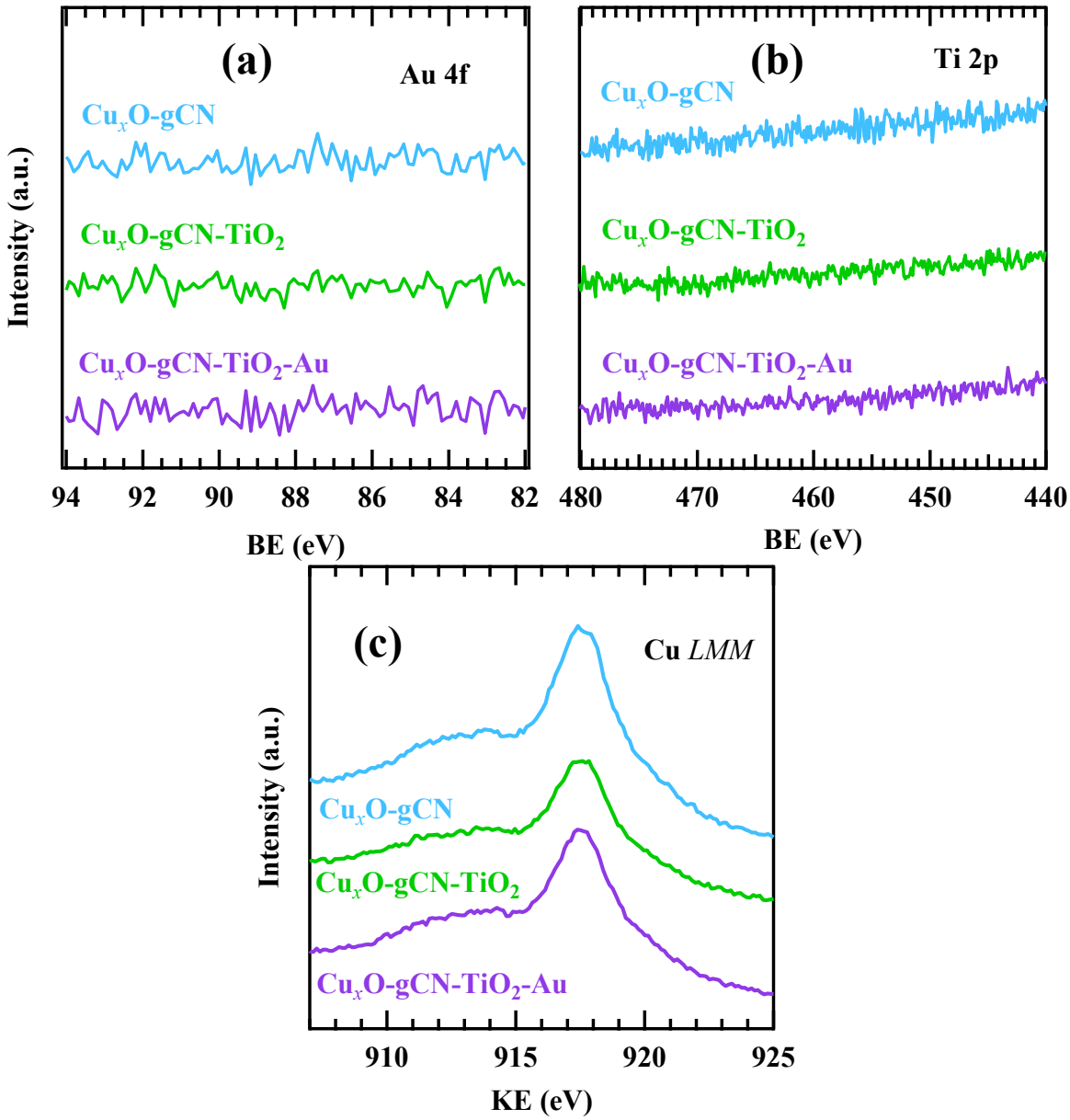

Fig. S6. Au 4f (a), Ti 2p (b) and Cu *LMM* Auger (c) signals for the indicated specimens.

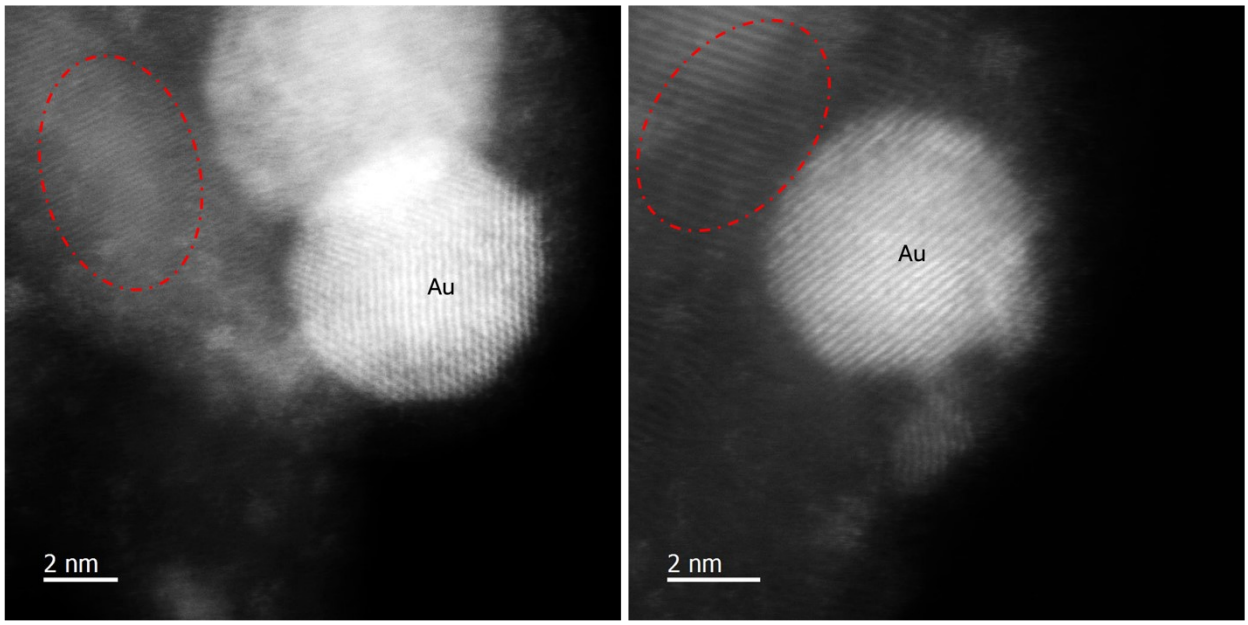

Fig. S7. Atomic resolution STEM ADF images showing lattice fringes in areas close to Au nanoparticles, as indicated by the dashed red circles. The lattice fringe distances are consistent with those of TiO_2.

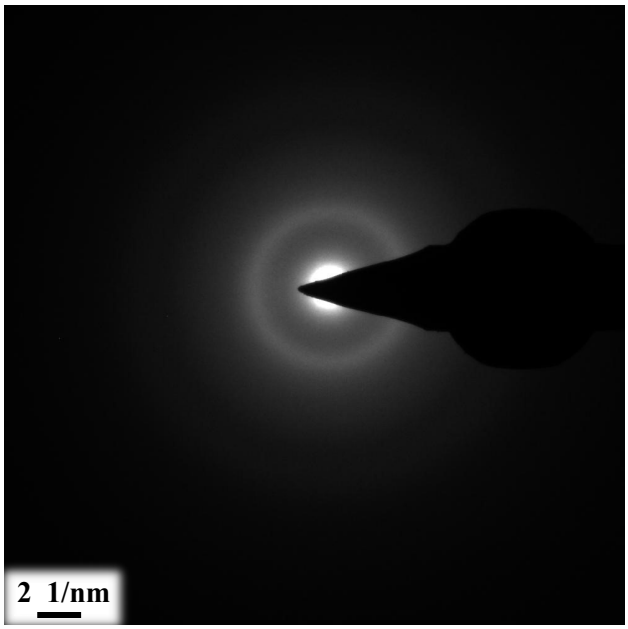

Fig. S8. An electron diffraction pattern acquired from gCN area in the target specimens. The diffused rings in the pattern show that graphitic caron nitride is amorphous.

§ S-2.2. Functional tests and related analyses

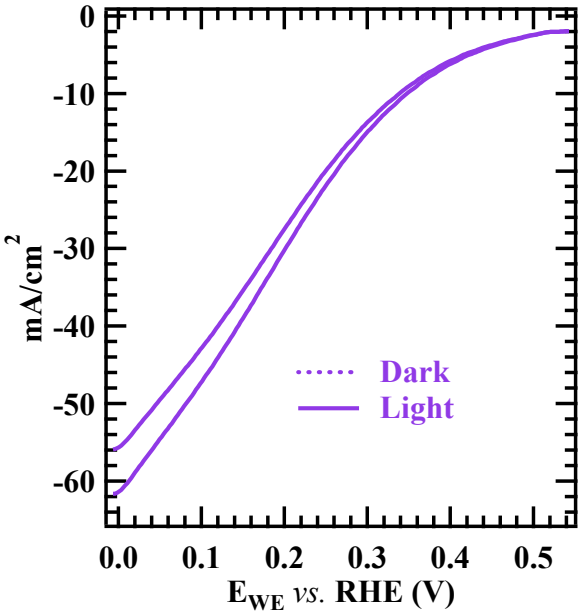

Fig. S9. Linear sweep voltammetry recorded for sample Cu_xO-gCN-TiO_2-Au collected in the dark and under illumination.

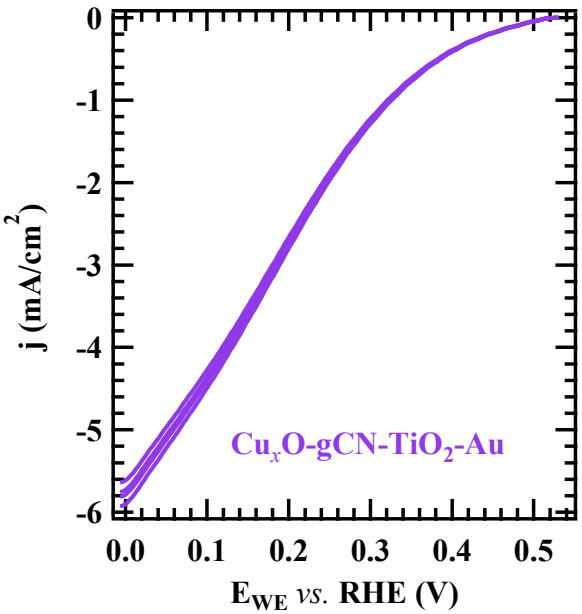

Fig. S10. Photocurrent *vs*. bias for four replicas of sample Cu_xO-gCN-TiO_2-Au, the best performing one. As can be observed, no appreciable current density variations were detected, demonstrating the repeatability of the results.

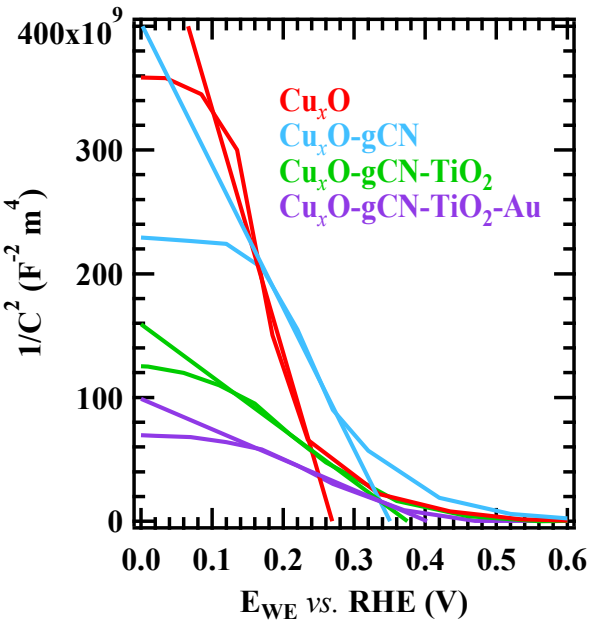

Fig. S11. Mott-Schottky plots at 1 KHz as a function of the applied bias for the investigated electrocatalysts. Experimental and fitting curves correspond to dashed and continuous lines, respectively.

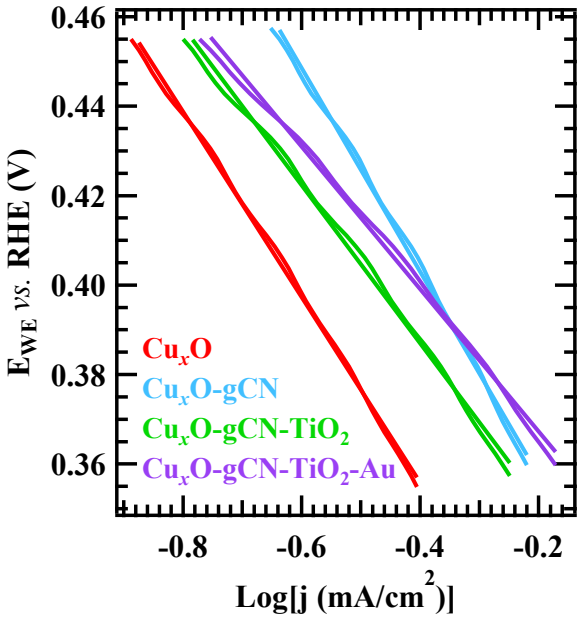

Fig. S12. Tafel plot for the target samples obtained from the LSV curves reported in Fig. 4a. Dashed and continuous lines indicate experimental and fitting curves, respectively.

Sample	Electrolyte	j_0 (mA/cm^2)	$ABPE_{max}$ (%)	E_{Wmax} (V_{RHE})	Tafel slope (mV/dec)
Cu_xO	$KHCO_3$ 0.5 M	-2.68	1	0.19	-227
Cu_xO-gCN		-3.86	2.17	0.20	-207
Cu_xO-gCN-TiO_2		-4.58	2.42	0.19	-177
Cu_xO-gCN-TiO_2-Au		-5.73	2.92	0.19	-160

Table S1. Hydrogen evolution reaction (HER) performances for the fabricated specimens. j_0 corresponds to the photocurrent density measured at 0.0 V *vs*. RHE. $ABPE_{max}$ values correspond to the maximum efficiency in each of the applied bias photon-to-current efficiency (ABPE) curves in Fig. 4c, normalized with respect to bare Cu_xO. E_{Wmax} is the corresponding potential value *vs*. RHE.

Material	Electrolyte	j_0 (mA/cm^2)	$ABPE_{max}$ (%)	E_{Wmax} (V_{RHE})	Tafel slope (mV/dec)	Ref.
Cu_2O	Na_2SO_4 1.0 M + HCOOH 0.5 M	≈ -2.0	*n.a.*	*n.a.*	*n.a.*	[16]
Cu_2O	H_2SO_4 0.025 M	≈ 0	*n.a.*	*n.a.*	*n.a.*	[17]
Cu_2O	Na_2SO_4 0.1 M	≈ -0.28 [a]	*n.a.*	*n.a.*	*n.a.*	[18]
Cu_2O		≈ -0.02 [b]	*n.a.*	*n.a.*	*n.a.*	[19]
Cu_2O	Na_2SO_4 0.2 M	≈ -0.09	*n.a.*	*n.a.*	*n.a.*	[20]
Cu_2O	Na_2SO_4 0.5 M	≈ -0.14	0.12	0.05	*n.a.*	[21]
Cu_2O	Na_2SO_4 0.5 M at *pH* = 4.9	≈ -0.51	0.02	0.18	*n.a.*	[6]
Cu_2O	Na_2SO_4 1.0 M	≈ -2.23 [c]	*n.a.*	*n.a.*	*n.a.*	[22]
Dual Cu_2O	Na_2SO_4 0.5 M + KH_2PO_4 0.1 M	≈ -7.0	1.9	0.45	*n.a.*	[23]
Pt-Cu_2O [d]	Na_2SO_4 0.1 M	≈ -1.1	*n.a.*	*n.a.*	*n.a.*	[24]
CuO	H_2SO_4 0.025 M	≈ 0	*n.a.*	*n.a.*	*n.a.*	[17]
CuO	Na_2SO_4 1.0 M + HCOOH 0.5 M	≈ -1.2	*n.a.*	*n.a.*	*n.a.*	[16]

Material	Electrolyte	j_0 (mA/cm^2)	$ABPE_{max}$ (%)	E_{Wmax} (V_{RHE})	Tafel slope (mV/dec)	Ref.
CuO	Na_2SO_4 0.1 M	≈ -0.46	0.08	0.24	*n.a.*	[10]
CuO [e]		≈ -0.80	*n.a.*	*n.a.*	*n.a.*	[25]
CuO		≈ -0.35 [a]	*n.a.*	*n.a.*	*n.a.*	[18]
CuO [f]		≈ -1.2	*n.a.*	*n.a.*	*n.a.*	[9]
CuO		≈ -0.45	*n.a.*	*n.a.*	*n.a.*	[26]
CuO		≈ -2.18	*n.a.*	*n.a.*	*n.a.*	[27]
CuO		≈ -0.25 [b]	*n.a.*	*n.a.*	*n.a.*	[19]
CuO		≈ -0.76	*n.a.*	*n.a.*	*n.a.*	[28]
CuO	Na_2SO_4 0.2 M	≈ -0.90	*n.a.*	*n.a.*	*n.a.*	[20]
CuO	Na_2SO_4 0.5 M	≈ -1.28	0.43	0.10	*n.a.*	[21]
CuO		-0.92	*n.a.*	*n.a.*	*n.a.*	[29]
Pt-CuO	Na_2SO_4 1.0 M	≈ -1.15	*n.a.*	*n.a.*	*n.a.*	[30]
CuO-Cu_2O [g]	Na_2SO_4 1.0 M + HCOOH 0.5 M	≈ -4.5	*n.a.*	*n.a.*	*n.a.*	[16]

Material	Electrolyte	j_0 (mA/cm²)	$ABPE_{max}$ (%)	E_{Wmax} (V_{RHE})	Tafel slope (mV/dec)	Ref.
CuO-Cu_2O	Na_2SO_4 0.1 M	≈ -0.62	*n.a.*	*n.a.*	*n.a.*	31
CuO-Cu_2O [g]	Na_2SO_4 1.0 M	≈ -0.14	*n.a.*	*n.a.*	*n.a.*	32
CuO/Cu_2O [h]	Na_2SO_4 0.2 M	≈ -1.01	*n.a.*	*n.a.*	*n.a.*	20
Cu_2O/CuO	Na_2SO_4 0.5 M	≈ -2.6	0.55	0.05	*n.a.*	21
$Cu/Cu_2O/CuO$	Na_2SO_4 50 mM buffered at *pH* = 6.82	-1.54	*n.a.*	*n.a.*	*n.a.*	33
$Cu/Cu_2O/Cu(OH)_2$		-1.28	*n.a.*	*n.a.*	*n.a.*	
CuO/NiO	Na_2SO_4 0.5 M	-1.02	*n.a.*	*n.a.*	*n.a.*	29
$Cu_2O/SnO_2/RuO_2$	Na_2SO_4 0.5 M + KH_2PO_4 0.1 M	≈ -4.30	*n.a.*	*n.a.*	*n.a.*	34
(CuO/CuO:Al)/ZnO:Al/TiO_2/Au–Pd	Na_2SO_4 0.1 M	≈ -4.58	*n.a.*	*n.a.*	*n.a.*	35
TiO_2/CuO		≈ -0.53 [b]	*n.a.*	*n.a.*	*n.a.*	19
Cu/TiO_2	KOH 1.0 M	≈ -0.01	*n.a.*	*n.a.*	*n.a.*	36
Cu_2O/TiO_2	Na_2SO_4 0.5 M at *pH* = 4.9	≈ -1.15	0.12	0.22	*n.a.*	6
Cu_2O/TiO_2/NiFe	Na_2SO_4 0.5 M at *pH* = 4.9	≈ -2.67	0.27	0.18	*n.a.*	6

Material	Electrolyte	j_0 (mA/cm²)	$ABPE_{max}$ (%)	E_{Wmax} (V_{RHE})	Tafel slope (mV/dec)	Ref.
gCN/CuO	Na_2SO_4 0.1 M	≈ -0.65	0.12	0.24	*n.a.*	[10]
CuO/gCN	Phosphate buffer (*pH* = 7)	≈ -0.50 [i]	*n.a.*	*n.a.*	*n.a.*	[37]
gCN-CuO		≈ -0.40 [i]	*n.a.*	*n.a.*	*n.a.*	[38]
CuI@gCN-CuO [l]		≈ -0.50 [i]	*n.a.*	*n.a.*	*n.a.*	[38]
CuO/gCN	Na_2SO_4 0.1 M	≈ 10^{-4} [c]	*n.a.*	*n.a.*	-314	[39]
Pt-Cu_2O/gCN [d]		≈ -1.7	*n.a.*	*n.a.*	*n.a.*	[24]
gCN/CuO		≈ -1.63	*n.a.*	*n.a.*	*n.a.*	[28]
gCN/C-CuO		≈ -2.37	*n.a.*	*n.a.*	*n.a.*	[28]
Cu_2O/TiO_2/rGO/NiFe [m]	Na_2SO_4 0.5 M at *pH* = 4.9	≈ -3.18	0.41	0.25	*n.a.*	[6]

Table S2. HER performances of selected (photo)electrocatalysts based on bare Cu_xO (*x*=1,2) and related composites. j_0 is defined as in Table S1. *n.a.* = not available. [a] @ ≈ 0.04 V *vs*. RHE. [b] @ ≈ -0.20 V *vs*. RHE. [c] @ ≈ 0.24 V *vs*. RHE. [d] Cu_2O foam. [e] porous pyramids. [f] film thickness = 150 nm. [g] biphasic thin film. [h] heterojunction structure. [i] @ ≈ 0.06 V *vs*. RHE. [l] with a metallic Cu underlayer. [m] rGO = reduced graphene oxide.

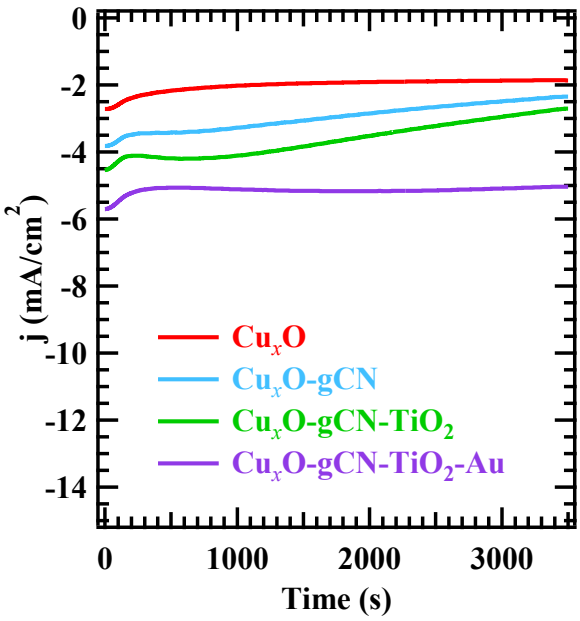

Fig. S13. Chronoamperometric (CA) traces for the investigated electrocatalysts, recorded at 0.0 V *vs.* RHE.

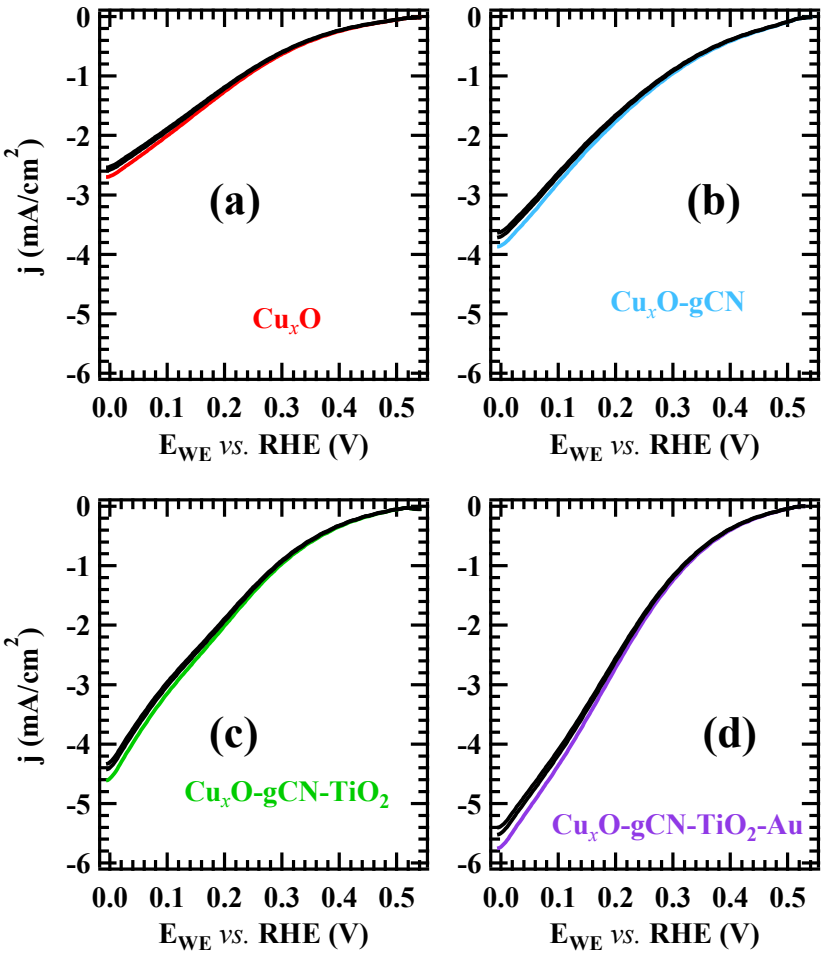

Fig. S14. LSV curves recorded on as-prepared samples (solid lines) and collected every 90 days for six months upon specimen storage under ambient conditions (dashed lines).

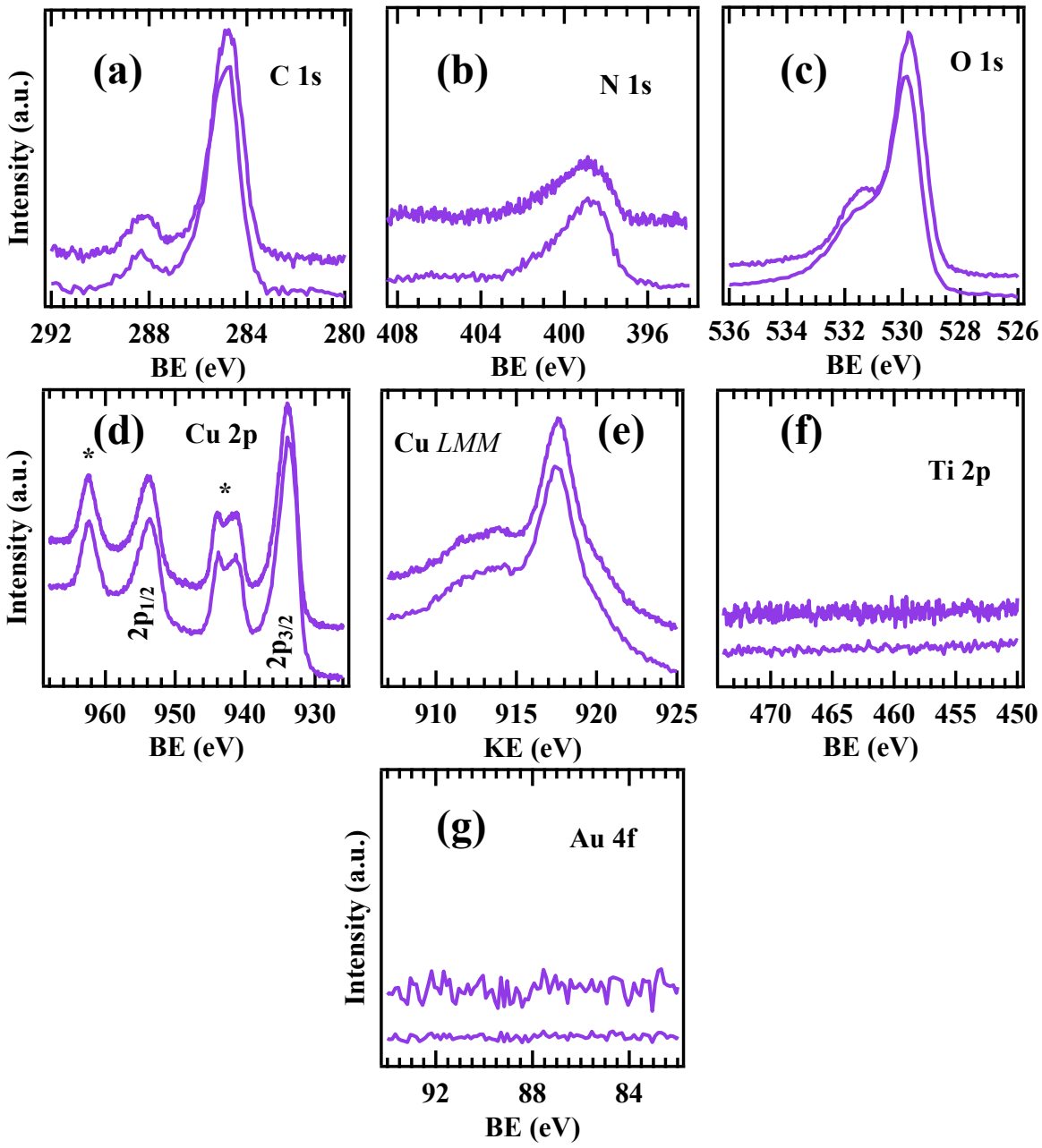

Fig. S15. XPS photopeaks for Cu_xO-gCN-TiO_2-Au before (solid line) and after storage under ambient conditions for six months, during which the specimen was subjected to photoelectrochemical tests every 90 days. The dotted line spectra reported herein have been obtained at the end of these repeated tests. In (d), shake-up satellites are denoted by *.

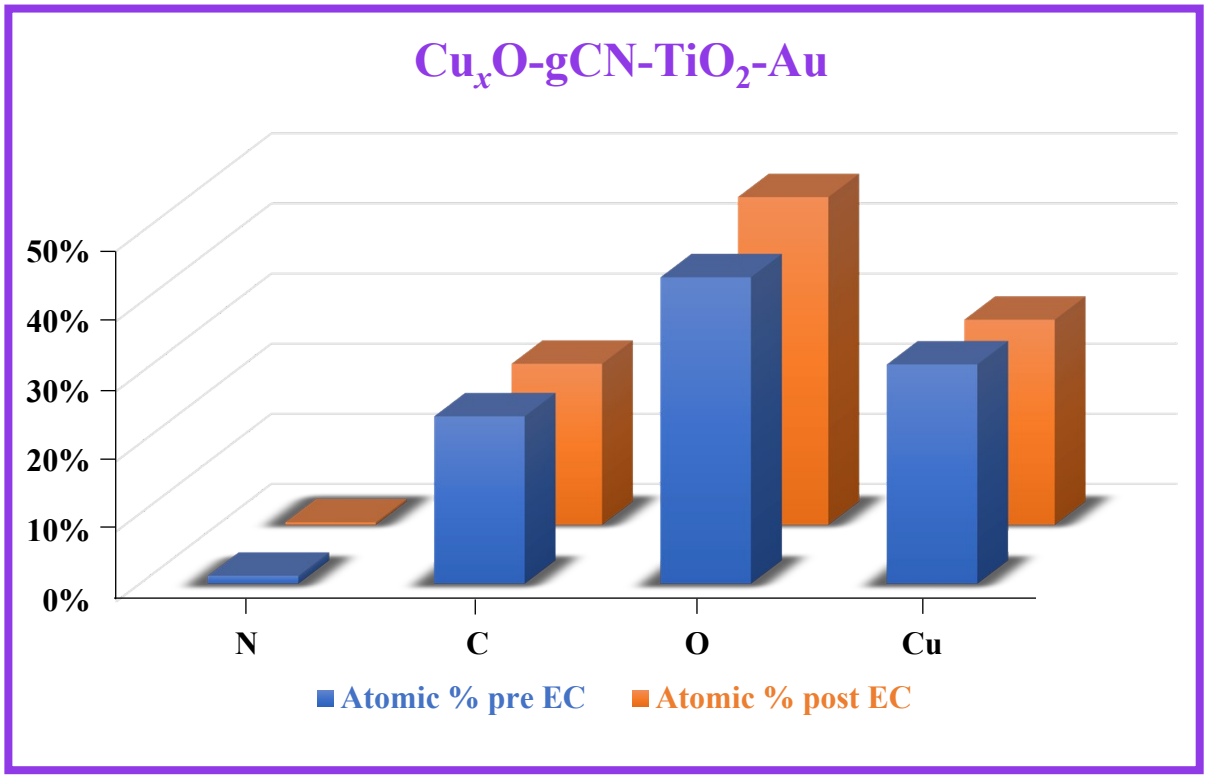

Fig. S16. XPS atomic percentage (%) values for Cu_xO-gCN-TiO_2-Au before photoelectrochemical tests (pre EC, in blue), and after storage under ambient conditions for six months, during which each sample was subjected to photoelectrochemical tests every 90 days (post EC, in orange). The post EC data reported herein have been obtained at the end of these repeated tests.

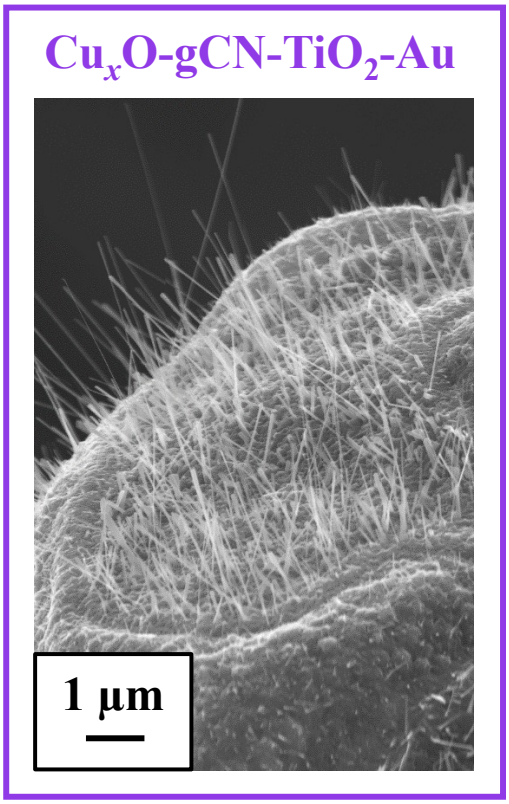

Fig. S17. FE-SEM micrographs for Cu_xO-gCN-TiO_2-Au after storage under ambient conditions for six months, during which the sample was subjected to photoelectrochemical tests every 90 days.

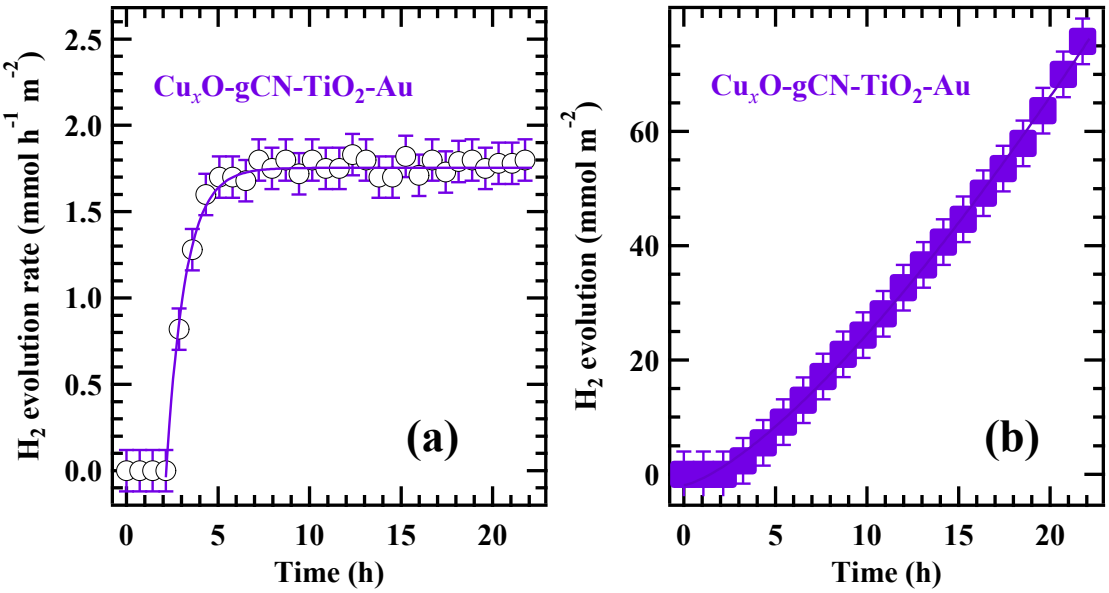

Fig. S18. (a) H_2 evolution rate and (b) integrated H_2 production obtained by photoreforming of 1:1 water-ethanol solutions on a Cu_xO-gCN-TiO_2-Au sample under simulated solar illumination.

Preliminary tests on hydrogen photogeneration in the absence of any external bias were carried out by photoreforming of water-ethanol solutions on Cu_xO-gCN-TiO_2-Au, the best performing specimen in photoelectrochemical experiments (compare Fig. 4 in the main paper text and related comments). In the case of mixtures of water and oxygenated organic compounds (*e.g.* ethanol, glucose, glycerol…), photoreforming takes place instead of the simple water splitting. The process involves the partial or complete oxidation of organics (depending on experimental conditions), such species being more easily oxidized than water.[40, 41] In the case of complete oxidation, the photoreforming process can be described by the following general reaction:

$$C_nH_mO_k + (2n - k)\ H_2O \rightarrow n\ CO_2 + (2n + m/2 - k)\ H_2 \qquad \text{(S6)}$$

The bias-free H_2 evolution performances of Cu_xO-gCN-TiO_2-Au obtained in the present work were higher than those afforded by various homologous photocatalysts reported so far in previous studies:

i) Cu_2O-TiO_2;[42]

ii) gCN-TiO_2;[43-47]

iii) gCN-Cu_2O;[48]

iv) gCN-CuO;[49]

v) gCN-CuO-TiO_2;[50]

vi) gCN-Cu_2O-TiO_2;[51]

vii) gCN-TiO_2-Au;[52]

viii) gCN-TiO_2-Pt.[53, 54]

§ S-3. References

1. L. Armelao, D. Barreca, M. Bertapelle, G. Bottaro, C. Sada and E. Tondello, *Thin Solid Films*, 2003, **442**, 48-52.

2. D. Briggs and M. P. Seah, *Practical Surface Analysis: Auger and X-ray Photoelectron Spectroscopy*, 2nd ed., New York, NY: Wiley, 1990.

3. L. Bigiani, T. Andreu, C. Maccato, E. Fois, A. Gasparotto, C. Sada, G. Tabacchi, D. Krishnan, J. Verbeeck, J. R. Morante and D. Barreca, *J. Mater. Chem. A*, 2020, **8**, 16902-16907.

4. L. Bigiani, C. Maccato, T. Andreu, A. Gasparotto, C. Sada, E. Modin, O. I. Lebedev, J. R. Morante and D. Barreca, *ACS Appl. Nano Mater.*, 2020, **3**, 9889-9898.

5. M. Benedet, A. Gallo, C. Maccato, G. A. Rizzi, D. Barreca, O. I. Lebedev, E. Modin, R. McGlynn, D. Mariotti and A. Gasparotto, *ACS Appl. Mater. Interfaces*, 2023, **15**, 47368-47380.

6. Y. Wang, S. Cao, Y. Huan, T. Nie, Z. Ji, Z. Bai, X. Cheng, J. Xi and X. Yan, *Appl. Surf. Sci.*, 2020, **526**, 146700.

7. M. Benedet, G. A. Rizzi, O. I. Lebedev, V. Roddatis, C. Sada, J.-L. Wree, A. Devi, C. Maccato, A. Gasparotto and D. Barreca, *J. Mater. Chem. A*, 2023, **11**, 21595-21609.

8. D. Barreca, G. Carraro, A. Gasparotto, C. Maccato, C. Sada, A. P. Singh, S. Mathur, A. Mettenbörger, E. Bontempi and L. E. Depero, *Int. J. Hydrogen Energy*, 2013, **38**, 14189-14199.

9. S. Masudy-Panah, R. Siavash Moakhar, C. S. Chua, A. Kushwaha and G. K. Dalapati, *ACS Appl. Mater. Interfaces*, 2017, **9**, 27596-27606.

10. H. Bae, V. Burungale, W. Na, H. Rho, S. H. Kang, S.-W. Ryu and J.-S. Ha, *RSC Adv.*, 2021, **11**, 16083-16089.

11. G. Carraro, C. Maccato, A. Gasparotto, T. Montini, S. Turner, O. I. Lebedev, V. Gombac, G. Adami, G. Van Tendeloo, D. Barreca and P. Fornasiero, *Adv. Funct. Mater.*, 2014, **24**, 372-378.

12. C. Maccato, D. Barreca, G. Carraro, A. Gasparotto, V. Gombac and P. Fornasiero, *Surf. Coat. Technol.*, 2013, **230**, 219-227.

13. Pattern N° 4-836, JCPDS (2000).

14. Pattern N° 5-667, JCPDS (2000).

15. Pattern N° 45-937, JCPDS (2000).

16. P. P. Kunturu and J. Huskens, *ACS Appl. Energy Mater.*, 2019, **2**, 7850-7860.

17. A. Aktar, S. Ahmmed, J. Hossain and A. B. M. Ismail, *ACS Omega*, 2020, **5**, 25125-25134.

18. Y.-F. Lim, C. S. Chua, C. J. J. Lee and D. Chi, *Phys. Chem. Chem. Phys*, 2014, **16**, 25928-25934.

19. W. Srevarit, S. Moonmangmee, P. Phapugrangkul, S. Kuboon, A. Klamchuen, N. Saito and C. Ponchio, *J. Alloys Compd.*, 2021, **859**, 157818.

20. T.-H. Yin, B.-J. Liu, Y.-W. Lin, Y.-S. Li, C.-W. Lai, Y.-P. Lan, C. Choi, H.-C. Chang and Y. Choi, *Coatings*, 2022, **12**, 1839.

21. Y. Yang, D. Xu, Q. Wu and P. Diao, *Sci. Rep.*, 2016, **6**, 35158.

22. A. Paracchino, V. Laporte, K. Sivula, M. Grätzel and E. Thimsen, *Nat. Mater.*, 2011, **10**, 456-461.

23. W. Niu, T. Moehl, W. Cui, R. Wick-Joliat, L. Zhu and S. D. Tilley, *Adv. Energy Mater.*, 2018, **8**, 1702323.

24. X. Ma, J. Zhang, B. Wang, Q. Li and S. Chu, *Appl. Surf. Sci.*, 2018, **427**, 907-916.

25. M. Basu, *ChemPhotoChem*, 2019, **3**, 1254-1262.

26. S. Masudy-Panah, R. S. Moakhar, C. S. Chua, A. Kushwaha, T. I. Wong and G. K. Dalapati, *RSC Adv.*, 2016, **6**, 29383-29390.

27. S. Masudy-Panah, R. Siavash Moakhar, C. S. Chua, H. R. Tan, T. I. Wong, D. Chi and G. K. Dalapati, *ACS Appl. Mater. Interfaces*, 2016, **8**, 1206-1213.

28. S. M. Hosseini H, R. Siavash Moakhar, F. Soleimani, S. K. Sadrnezhaad, S. Masudy-Panah, R. Katal, A. Seza, N. Ghane and S. Ramakrishna, *Appl. Surf. Sci.*, 2020, **530**, 147271.

29. H. L. S. Santos, P. G. Corradini, M. A. S. Andrade and L. H. Mascaro, *J. Solid State Electrochem.*, 2020, **24**, 1899-1908.

30. J. Li, X. Jin, R. Li, Y. Zhao, X. Wang, X. Liu and H. Jiao, *Appl. Catal., B*, 2019, **240**, 1-8.

31. T. Xie, T. Zheng, R. Wang, Y. Bu and J.-P. Ao, *Green Energy Environ.*, 2018, **3**, 239-246.

32. R. Borkar, R. Dahake, S. Rayalu and A. Bansiwal, *J. Electron. Mater.*, 2018, **47**, 1824-1831.

33. Z. Zhang and P. Wang, *J. Mater. Chem.*, 2012, **22**, 2456-2464.

34. J. Azevedo, S. D. Tilley, M. Schreier, M. Stefik, C. Sousa, J. P. Araújo, A. Mendes, M. Grätzel and M. T. Mayer, *Nano Energy*, 2016, **24**, 10-16.

35. S. Masudy-Panah, Y. J. K. Eugene, N. D. Khiavi, R. Katal and X. Gong, *J. Mater. Chem. A*, 2018, **6**, 11951-11965.

36. L. M. Ombaka, M. Curti, J. D. McGettrick, M. L. Davies and D. W. Bahnemann, *ACS Appl. Mater. Interfaces*, 2020, **12**, 30365-30380.

37. S. Wojtyła and T. Baran, *Nano Select*, 2021, **2**, 389-397.

38. S. Wojtyła, K. Szmit and T. Baran, *J. Inorg. Organomet. Polym. Mater.*, 2018, **28**, 492-499.

39. W. Xue, W. Chang, X. Hu, J. Fan, X. Bai and E. Liu, *J. Colloid Interface Sci.*, 2020, **576**, 203-216.

40. D. Barreca, G. Carraro, V. Gombac, A. Gasparotto, C. Maccato, P. Fornasiero and E. Tondello, *Adv. Funct. Mater.*, 2011, **21**, 2611-2623.

41. M. Cargnello, A. Gasparotto, V. Gombac, T. Montini, D. Barreca and P. Fornasiero, *Eur. J. Inorg. Chem.*, 2011, **2011**, 4309-4323.

42. S. Lv, Y. Wang, Y. Zhou, Q. Liu, C. Song and D. Wang, *J. Alloys Compd.*, 2021, **868**, 159144.

43. A. Alsalme, A. H. Galal, E. F. El-Sherbeny, A. Soltan, M. F. Abdel-Messih and M. A. Ahmed, *Diamond Relat. Mater.*, 2022, **122**, 108819.

44. W. Liu, S. Chang, D. Liu and F. Wen, *Colloids Surf., A*, 2021, **609**, 125681.

45. I. M. Sundaram, S. Kalimuthu, G. P. P, K. Sekar and S. Rajendran, *Int. J. Hydrogen Energy*, 2022, **47**, 3709-3721.

46. J. Pan, Z. Dong, B. Wang, Z. Jiang, C. Zhao, J. Wang, C. Song, Y. Zheng and C. Li, *Appl. Catal., B*, 2019, **242**, 92-99.

47. Q. Tay, X. Wang, X. Zhao, J. Hong, Q. Zhang, R. Xu and Z. Chen, *J. Catal.*, 2016, **342**, 55-62.

48. M. Alhaddad, R. M. Navarro, M. A. Hussein and R. M. Mohamed, *J. Mater. Res. Technol.*, 2020, **9**, 15335-15345.

49. Q. Zhang, Y. Li, J. Zhong and J. Li, *Fuel*, 2023, **353**, 129224.

50. B. Chen, J. Yu, R. Wang, X. Zhang, B. He, J. Jin, H. Wang and Y. Gong, *Sci. China Mater.*, 2022, **65**, 139-146.

51. L. Dai, F. Sun, P. Fu and H. Li, *RSC Adv.*, 2022, **12**, 13381-13392.

52. R. A. Rather, S. Singh and B. Pal, *Appl. Catal., B*, 2017, **213**, 9-17.

53. M. A. Alcudia-Ramos, M. O. Fuentez-Torres, F. Ortiz-Chi, C. G. Espinosa-González, N. Hernández-Como, D. S. García-Zaleta, M. K. Kesarla, J. G. Torres-Torres, V. Collins-Martínez and S. Godavarthi, *Ceram. Int.*, 2020, **46**, 38-45.

54. M. R. Gholipour, F. Béland and T.-O. Do, *Int. J. Chem. Reactor Eng.*, 2016, **14**, 851-858.